

Numerical investigation of turbulent flow over a stationary and oscillatory NACA0012 airfoil using overset grids method

M. J. Vafaei Rostami^{1,*},[†], M. Saghafian^{1,‡}, A. Sedaghat^{1,‡} and Mo. Miansari²

¹*Mechanical Engineering Department, Isfahan University of Technology, Isfahan, Iran*

²*Mechanical Engineering Department, Babol Noshirvani University of Technology, Babol, Iran*

SUMMARY

In this numerical study, unsteady and incompressible turbulent flows have been considered around stationary and flapping NACA0012 airfoil. Overset grid technique is used in this work. Three turbulence models have been examined including the linear Launder–Sharma $k-\varepsilon$ model, nonlinear Craft–Launder–Suga $k-\varepsilon$ model and nonlinear Lien–Chen–Leschziner $k-\varepsilon$ model.

First, the flow field around a stationary airfoil is solved for validating purposes. The results reveal different capabilities of capturing separation angle of attack using linear and nonlinear models. Nonlinear models predict smaller stall angle compared with the linear ones.

Second, the flow field around a plunging airfoil is considered at various angles of attack, reduced frequencies and different amplitudes. The results show that the effects of reduced frequency are highly significant. There are differences in aerodynamic forces and wake structures in the upstroke and the down stroke motions, because they are functions of the mean angle of attack, oscillation amplitude and reduced frequency. Copyright © 2010 John Wiley & Sons, Ltd.

Received 23 July 2009; Revised 16 February 2010; Accepted 17 February 2010

KEY WORDS: stall; oscillatory airfoil; flow patterns; linear and nonlinear $k-\varepsilon$ models; overset grids

1. INTRODUCTION

Unsteady aerodynamic phenomena occur in modern fluid dynamic such as helicopters, Micro air vehicles (MIVs), turbines and turbo-machines and so on. Experiments show that time-dependent dynamic forces of helicopters' rotor blades, plane blades, wind turbines and high-performance airplanes are greater than static forces in different conditions. The theory of unsteady aerodynamics for oscillatory airfoils was first focused on as an efficient solution to solve the Flutter problem. This theory was then used widely in biofluid dynamic since the forward movement of birds, insects and fish is justifiable using this theory.

Earlier studies of oscillatory airfoils were conducted by Glauert [1]. However, a more detailed analysis of the issue was carried out by Theodorsen and Garrick [2] and is the basis for many aerodynamic analyses with the assumption of incompressible inviscid flow and low oscillation amplitude. Although successful efforts have been made to determine stagnant aerodynamic coefficients in steady flow in engineering sections by using numerical and empirical methods, there is still much to do in unsteady aerodynamics and determining aerodynamic coefficients in this condition. Some experimental studies in this field include Breton *et al.*'s [3] in 1997 who worked on

*Correspondence to: M. J. Vafaei Rostami, Mechanical Engineering Department, Isfahan University of Technology, Isfahan, Iran.

[†]E-mail: mjvafaeirostami@yahoo.com

[‡]Assistant Professor.

qualitative and quantitative study of the physics of separable flows around the NACA0012 airfoil in pitching oscillation, which undergoes stall. In 1998, Panda and Zaman [4] empirically studied an airfoil under pitching oscillation. The Reynolds number was 22 000 and 44 000 based on the chord. The pitching oscillation was applied in a sine manner for the NACA0012 section. Tuncer's studies [5] in 1986 are examples of numerical studies. He studied unsteady flow fields around oscillatory airfoils in pitching oscillation and also studied dynamic stall. He used a two-layer algebraic turbulence model. In 1997, he studied a plunging oscillation airfoil using the overset grids technique [6] and compared the results with the single grid model. He used the Baldwin–Barth turbulent model. Calculations were done in the Reynolds number of 3×10^6 and the Mach number of 0.3. In 1998, Guilmineau and Queutey [7] studied dynamic stall under pitching oscillation on several wing sections such as NACA0012. They used Baldwin–Barth and SST $k-\omega$ models for turbulence modeling. In 1999, Baracos and Drikakis [8] studied turbulent flow around the NACA0015 airfoil under pitching oscillation. The Baldwin–Lomax turbulent model was used and different stall states were studied. In 2000, Tuncer and Platzer [9] studied the flow around an airfoil with simultaneous pitching and plunging oscillation. They studied the process of vortex formation and flow separation. They used a dynamic grid and the simple algebraic turbulent model of Baldwin–Lomax. Also in 2003, Akbari and Price [10] simulated dynamic stall in pitching oscillation using the vortex method. In that study, they studied the effect of several parameters such as reduced frequency, Reynolds number and incidence angle. The vortex method was used in the vorticity flow function form to solve Navier–Stokes equations. Their results showed that reduced frequency has a greater effect on flow field than other parameters. In 2004, Oo *et al.* [11] empirically studied vortex structure and flow wake around an oscillatory airfoil. The Reynolds number was 1000 in their experiments and they did not mention force coefficients in their studies.

In stationary airfoils, although Gregory measurements are the empirical data available for aerodynamic characteristics [12], we can also point to some other empirical researches like Abott and Doenhoff [13], Michos *et al.* [14] and Sheldahl and Klimas [15], which are all used for comparison in this article. Milas numerical results [16] are also used to compare lift, drag and pressure coefficients.

In this article, the unsteady 2D incompressible flow is simulated around a stationary and oscillatory symmetric ACA0012 airfoil at Reynolds numbers of 7×10^5 , 1×10^6 and 3×10^6 using overset grids method. Linear and nonlinear Low Reynolds models of $k-\varepsilon$ are used to model turbulence. These models include the linear model of Launder–Sharma (LS) [17] and the nonlinear models of Craft–Launder–Suga (CLS) [18] and Lien–Chen–Leschziner (LCL) [19]. In this research, nonlinear turbulence models are used for the first time using overset grids method to study the incompressible flow. Reviewing previous studied, it seems that the nonlinear model has not been used in analyzing any problem. The developed CFD code in this research, which uses the overset grids technique, can now be used to study flow around a bunch of airfoils or compound airfoils in dynamic relative motion to each other.

2. GOVERNING EQUATIONS IN TURBULENT FLOWS AND MODELS

Averaged equations of Navier–Stokes governing the unsteady incompressible flow are

$$\frac{\partial U_i}{\partial x_i} = 0 \quad (1)$$

$$\frac{\partial U_i}{\partial t} + U_j \frac{\partial U_i}{\partial x_j} = -\frac{1}{\rho} \frac{\partial P}{\partial x} + \frac{\partial}{\partial x_j} \left(\nu \frac{\partial^2 U_i}{\partial x_j^2} - \overline{u_i' u_j'} \right) \quad (2)$$

where p , ρ , U_i are stress, density and flow velocity, respectively. $\overline{u_i' u_j'}$ is the Reynolds stress term, which should be modeled. Linear and nonlinear models of $k-\varepsilon$ are used for Reynolds stress terms in this article.

Table I. Coefficients for turbulent models.

| Lauder–Sharma (LS) | | Craft–Lauder–Suga (CLS) | Lien–Chen–Leschziner (LCL) |
|----------------------|--|---|--|
| $C_{\varepsilon 1}$ | 1.44 | 1.44 | 1.44 |
| $C_{\varepsilon 2}$ | 1.92 | 1.92 | 1.92 |
| σ_k | 1.0 | 1.0 | 1.0 |
| σ_ε | 1.3 | 1.3 | 1.3 |
| C_μ | 0.09 | $\frac{0.1}{1+0.35\eta^{3/2}}(1-\exp(-0.36e^{-0.75\eta}))$ | $\frac{2/3}{1.25+\bar{S}+0.9\bar{\Omega}}$ |
| C_1 | 0 | $-0.4c_\mu f_\mu$ | $3f_\mu/(1000+\bar{S}^3)$ |
| C_2 | 0 | $0.4c_\mu f_\mu$ | $15f_\mu/(1000+\bar{S}^3)$ |
| C_3 | 0 | $1.04c_\mu f_\mu$ | $19f_\mu/(1000+\bar{S}^3)$ |
| C_4 | 0 | $80c_\mu^3 f_\mu$ | $80c_\mu^3 f_\mu$ |
| C_5 | 0 | 0 | 0 |
| C_6 | 0 | $-40c_\mu^3 f_\mu$ | $-16c_\mu^3 f_\mu$ |
| C_7 | 0 | $40c_\mu^3 f_\mu$ | $16c_\mu^3 f_\mu$ |
| <i>Low-Re terms</i> | | | |
| f_μ | $\exp\left(\frac{-3.4}{(1+R_t/50)^2}\right)$ | $1-\exp[-(R_t/90)^2-(R_t/400)^2]$ | $\frac{1-\exp(-0.0198y^*)}{(1+2\kappa/c_\mu^{3/4}y^*)^{-1}}$ |
| f_1 | 1.0 | 1.0 | 1.0 |
| f_2 | $1-0.3\exp(-R_t^2)$ | $1-0.3\exp(-R_t^2)$ | $1-0.3\exp(-R_t^2)$ |
| D | $2\nu\left(\frac{\partial k^{1/2}}{\partial x_i}\right)^2$ | $2\nu\left(\frac{\partial k^{1/2}}{\partial x_i}\right)^2$ | 0 |
| | | | YAP, ($R_t \leq 250$) |
| E | $2\nu\nu_t\left(\frac{\partial^2 U_i}{\partial x_j \partial x_k}\right)^2$ | $0.0022\frac{\bar{S}\nu_t k^2}{\bar{\varepsilon}}\left(\frac{\partial^2 U_i}{\partial x_j \partial x_k}\right)^2 + YAP, (R_t \geq 250)$ | $C_{\varepsilon 2} f_2 \frac{\varepsilon^l}{k} \exp(-0.00375y^{*2})$ |

$$R_t = (k^2/(\nu\bar{\varepsilon}))\nu\bar{\varepsilon}, \quad y^* = y_n k^{3/2}/\nu, \quad \bar{S} = (k/\varepsilon)\sqrt{2S_{ij}S_{ij}}, \quad \bar{\Omega} = (k/\varepsilon)\sqrt{2\Omega_{ij}\Omega_{ij}}, \quad \eta = \text{Max}(\bar{S}, \bar{\Omega}).$$

$$YAP = \text{Max}(0.83(\gamma-1)\gamma^2(\bar{\varepsilon}/k), 0), \quad \gamma = k^{3/2}/c_l \bar{\varepsilon} y_n, \quad c_l = 2.5, \quad \varepsilon^l = (k^{3/2}/\kappa y_n)(C_\mu^{3/4} + 2\kappa/y^*).$$

It should be noted that the effects of linear acceleration in the non-inertial system and related to the minor grid are inserted into Navier–Stokes equations as the source term.

2.1. The LS linear model

The stress and strain relation is defined as

$$-\overline{u_i u_j} = \nu_t \left(\frac{\partial U_i}{\partial x_j} + \frac{\partial U_j}{\partial x_i} \right) - \frac{2}{3} k \delta_{ij} \tag{3}$$

where δ_{ij} represents the kronecker delta and ν_t is the turbulent kinetic viscosity, which is described as

$$\nu_t = C_\mu \frac{k^2}{\bar{\varepsilon}} \tag{4}$$

C_μ and f_μ coefficients are introduced in Table I. K represents turbulent kinetic energy and $\bar{\varepsilon}$ is homogenous part of dissipation rate (ε).

Transfer equations for k and $\bar{\varepsilon}$ are as follows:

$$\frac{Dk}{Dt} = \frac{\partial}{\partial x_i} \left[\left(\nu + \frac{\nu_t}{\sigma_k} \right) \frac{\partial k}{\partial x_i} \right] + P^{(K)} - \varepsilon \tag{5}$$

$$\frac{\partial \bar{\varepsilon}}{\partial t} + U_j \frac{\partial \bar{\varepsilon}}{\partial x_j} = \frac{\partial}{\partial x_j} \left[\left(\nu + \frac{\nu_t}{\sigma_\varepsilon} \right) \frac{\partial \bar{\varepsilon}}{\partial x_j} \right] + C_{\varepsilon 1} f_1 \frac{\bar{\varepsilon}}{k} P^{(k)} - C_{\varepsilon 2} f_2 \frac{\bar{\varepsilon}^2}{k} + E \tag{6}$$

E is described in Table I and P^K is the rate of turbulent kinetic energy and is defined as

$$P^{(k)} = -\overline{u'_i u'_j} \frac{\partial \bar{u}_i}{\partial x_j} \quad (7)$$

Also for homogenous and non-homogenous dissipation rate, we have

$$\bar{\varepsilon} = \varepsilon - D \quad (8)$$

where D is defined in Table I.

2.2. LCL and CLC nonlinear models

In nonlinear models, the relationship between strain and vorticity (with regard to second- and third-order phrases as follows) is derived from the following:

$$\begin{aligned} \rho \overline{u_i u_j} = & \frac{2}{3} k \delta_{ij} - 2c_\mu f_\mu \frac{k^2}{\varepsilon} s_{ij} + C_1 \frac{k^3}{\varepsilon^2} \left(S_{ik} S_{jk} - \frac{1}{3} S_{kl} S_{kl} S_{ij} \right) + C_2 \frac{k^3}{\varepsilon^2} (S_{ik} \Omega_{jk} - S_{jk} \Omega_{ik}) \\ & + C_3 \frac{k^3}{\varepsilon^2} \left(\Omega_{ik} \Omega_{jk} - \frac{1}{3} \Omega_{kl} \Omega_{kl} \delta_{ij} \right) + C_4 \frac{k^4}{\varepsilon^3} (S_{ik} \Omega_{jl} + S_{jk} \Omega_{il}) S_{kl} \\ & + C_5 \frac{k^4}{\varepsilon^3} \left(\Omega_{ik} \Omega_{kl} S_{lj} + \Omega_{jk} \Omega_{kl} S_{li} - \frac{2}{3} \Omega_{kl} S_{lm} \Omega_{mk} S_{ij} \right) \\ & + C_6 \frac{k^4}{\varepsilon^3} S_{kl} S_{kl} S_{ij} + C_7 \frac{k^4}{\varepsilon^3} \Omega_{kl} \Omega_{kl} S_{ij} \end{aligned} \quad (9)$$

Strain tensors and averaged vorticity are described as follows:

$$S_{ij} = \frac{1}{2} \left(\frac{\partial u_i}{\partial x_j} + \frac{\partial u_j}{\partial x_i} \right), \quad \Omega_{ij} = \frac{1}{2} \left(\frac{\partial u_i}{\partial x_j} - \frac{\partial u_j}{\partial x_i} \right) \quad (10)$$

Table I displays the coefficients for LS, CLS and LCL.

3. NUMERICAL SOLUTION

In this article, the solution method for discretizing the flow field is based on the finite-volume method and the SIMPLEC [20, 21] pressure correction algorithm is used to solve the flow field. The QUICK scheme [22] is used to calculate convection terms and the Crank–Nicolson method [23, 24] to calculate time alternation. The Rhi–Chow method [25] is used to prevent numerical and non-physical fluctuation in pressure and velocity fields. Moreover, the Hybrid method [26] is used in k and ε equations to avoid numerical instability.

4. OVERSET GRIDS METHOD

In the overset grids method, a background grid (major grid) (usually a simple rectangular grid) and a number of overset grids (minor grid) overlap the body. These grids should be able to transfer data between each other using an appropriate method. The flows equations in the main and overset grids are separately solved and the obtained data are exchanged in particular points by interpolating between main and overset grids. A background grid of H kind and an overset grid of C kind overlapping the body are used in this research (Figure 1). Those points of the background grid in which airfoil is located are regarded as rigid body and are called ‘Hole Points’. Obtained results in the overset grid are transferred to the adjacent points of the object in the background grid. These points of the background grid, which receive the results of solving the problem in the overset grid,

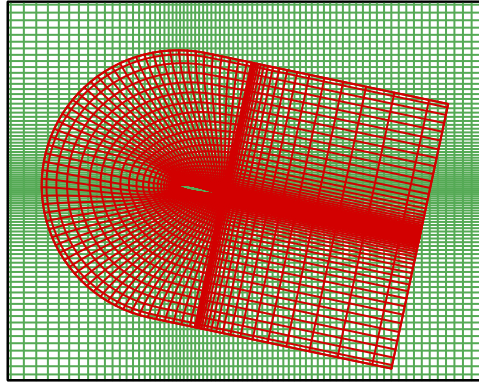


Figure 1. Both overset and background grids.

are called ‘fringe points’. On the other hand, the overset grid receives its required data in every time step through its exterior boundary points (which are called fringe) and by interpolating from the background grid. It is clear that a quick and simple algorithm should be used for locating the fringe points of a grid in another grid and interpolating data. In every time step, the main and the overset grids are solved in a repetitive loop, which includes the point searching process and data transfer before and after each grid is solved.

The overset grids method provides flow solution for different formations of objects near each other, dynamic objects and objects with too complicated geometries.

A considerable part of the idea of the overset grids method and the search algorithm applied in this article has been stated by Nirschl *et al.* [27], and Tuncer [6].

It should be mentioned that the overset grids method, which is applied to analyze flow field over a moving body, is implemented in the following manner:

The body fitted grid (overset grid) moves on stationary background grid and sits in a new position at each time step, and then flow field is analyzed. In other words, the overset grids are solved in a non-inertial coordinate system, whereas the background grids are always solved in an inertial system. Concerning the overset grids, effects of linear acceleration, indicating the motion of the body, is added to the Navier–Stokes equation as a source term (Equation (11)). It is evident that no term is added related to background grid, which is stationary.

$$\vec{a} = \frac{d^2 \vec{R}}{dt^2} \quad (11)$$

5. BOUNDARY CONDITIONS

In the inlet boundary of the background grid, inlet velocity value, turbulent kinetic energy, dissipation rate and also the turbulent viscosity to molecular viscosity ratio are defined. Convection boundary condition is applied for solving each parameter for the outlet boundary. Furthermore, velocity value, turbulent kinetic energy and dissipation rate are obtained through interposing adjacent points in the overset grid for those points in the background grid that are located near the airfoil surface.

In the overset grid, the no slip condition on the airfoil surface is used. The turbulent kinetic energy is zero on the surface and the Neuman condition is used for dissipation rate. Also, the existing values on the exterior boundary of the overset grid (fringe points of the overset grid) obtained by interpolating its adjacent nodes in the background grid are used as exterior boundary condition of this grid.

6. RESULTS AND DISCUSSION

In this section, general analysis of the airfoils in stationary and oscillatory states is to be discussed.

6.1. Stationary airfoil

In this part, numerical solution results are presented for the 2D and turbulent incompressible flow around a stationary NACA0012 airfoil in three Reynolds numbers of 7×10^5 , 1×10^6 and 3×10^6 and one low-Reynolds linear $k-\varepsilon$ model (LS) and two low-Reynolds nonlinear $k-\varepsilon$ models (CLS & LCL). Lift and drag aerodynamic coefficients, pressure coefficient on airfoil surfaces, counters of turbulent kinetic energy, the turbulent viscosity to molecular viscosity ratio, time alternations of energy coefficients in stall angle and following that, the effect of stall on pressure coefficient and finally flow patterns in angles before and after stall are all studied.

The grid effect was studied for the independence of solution from the number of points in grid; comparing results for lift and drag values, finally, a grid sized 142×122 for the background grid and a grid sized 102×82 for the overset grid were used. It should be mentioned that this research was conducted merely for the overset grid. Coefficient values of lift and drag forces were compared in the Reynolds number of 1×10^6 and a leading angle of 12° , as seen in Table II.

In Figure 2, coefficient values of lift and drag forces with different leading angles of airfoil in the Reynolds number of 3×10^6 are compared with the experimental results of Gregory and O'Riley [12], Abott and Doenhoff [13], Michos [14] and Sheldahl and Klimas [15] and also the numerical results of Milas [16]. As clearly seen in this comparison, experimental and numerical results are very close to each other for angles less than 10° ; however, the difference between values is revealed by the increase in leading angle. In this research, the nonlinear models of CLS and LCL predict the stall 1° earlier than the linear model of LS. It should be noted that the linear model of LS predicts the quick changes of the stall region smoother than other nonlinear models. The inability of the linear models of $k-\varepsilon$ to predict sudden changes of force coefficients coming from stall was also reported by Rizzetta and Visbal [28]. Figure 3 shows lift and drag coefficients according to the leading angle in three different Reynolds number and for the nonlinear model of CLS. With an increase in the Reynolds number, the stall leading angle is delayed as the flow momentum is fortified in the boundary layer against the undesired pressure gradient.

Therefore, in greater Reynolds number, greater values of lift force coefficients can be reached by increasing the leading angle, which is clear in the diagram. Figure 4 shows the pressure coefficient diagram on high and low surfaces of airfoil for the CLS model in the Reynolds number of 3×10^6 and a leading angle of 12° in comparison to the results of Gregory and Milas. It is obvious that the CLS model predicts higher pressure coefficient in the airfoil leading edge than the empirical and the numerical results; however, there is good consistency with the mentioned results except for airfoil leading edge. In Figure 5, the obtained results are compared with linear and nonlinear models for pressure coefficient. Apart from the airfoil leading edge, no significant difference is observed in pressure coefficient distribution in these three models.

In Figure 6, the counters of turbulent kinetic energy and the turbulent viscosity to molecular viscosity ratio are shown. As seen, the linear model of LS predicts the turbulent kinetic energy (k) and the turbulent viscosity to molecular viscosity ratio (μ_t/μ) in the stagnation region too highly and non-physically. This is due to the production of turbulent kinetic energy by the non-revolving

Table II. Overset grid study at $Re=10^6$ and $\alpha=12$ using LS model.

| C grid ($n_i \times n_j$) | C_L ($\Delta t=0.01$) | C_L ($\Delta t=0.005$) |
|-----------------------------|---------------------------|----------------------------|
| 102×52 | 1.240 | 1.245 |
| 102×82 | 1.235 | 1.239 |
| 142×52 | 1.2319 | 1.232 |
| 142×82 | 1.228 | 1.230 |
| 182×82 | 1.171 | 1.173 |

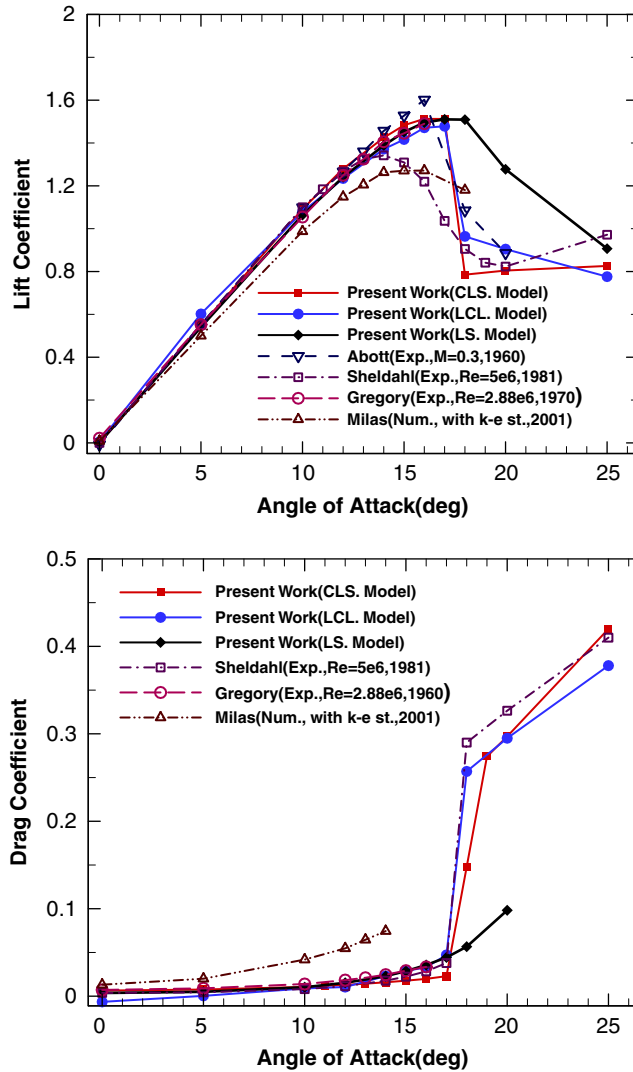


Figure 2. Lift and drag coefficients versus angles of attacks at $Re = 3 \times 10^6$.

strain and yields to non-physical and incorrect results. The transmission of this non-physical turbulence into the boundary layer affects the prediction of separation region and consequently the force coefficients. Hence, k and accordingly μ_t/μ are scattered over a broad band in the wake considerably. Using nonlinear models, intense and non-physical turbulence are not observed around the stagnation point.

6.1.1. Studying flow stall. Figure 7 shows the time change manners of lift and drag coefficients for three models in the Reynolds number of 1×10^6 and a leading angle of 16° (stall occurrence). In the linear model, the separation angle is postponed due to the overestimation of turbulence and vortex viscosity in the boundary layer. Therefore, the diagram of lift and drag coefficients will be completely flat after some time steps. In fact, the overestimation of μ_t in a flow intensifies the turbulent boundary layer and consequently, flow separation and then its resultant stall is delayed. In nonlinear models, a lower value is estimated for μ_t in comparison with the linear model by adding linear terms to boussinesq vortex viscosity and reducing k and accordingly μ_t wherever the average strain rate of the flow is high. Lower turbulent intensity in the boundary layer with nonlinear models causes the flow separation and the stall phenomenon occurs earlier. On one

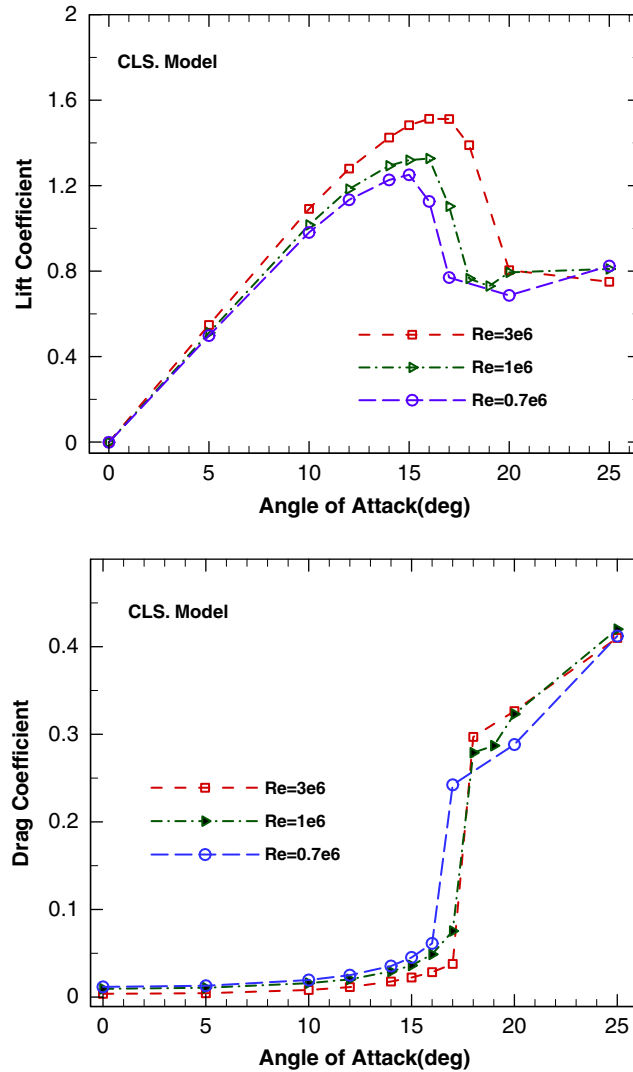


Figure 3. Lift and drag coefficients versus angles of attacks at different Reynolds numbers.

side, when stall occurs, vortex shedding (which is the direct result of stall) causes radical changes in pressure coefficient and consequently in lift and drag coefficients. This phenomenon has an oscillatory nature with specific frequency and amplitude; therefore, the diagrams of lift and drag coefficients will also have a repetitive oscillation. However, it should be noted that oscillations will be more repetitive by increasing the leading angle.

Figure 8 shows time alternations of lift and drag for the three models in the Reynolds number of 1×10^6 and a leading angle of 20° (after stall). As seen, the LS model estimates a lot less oscillation amplitude compared with the two other models, which is due to considering high non-physical value for turbulence viscosity, which causes oscillation dissipation in flow. The CLS model shows a non-harmonic oscillation, whereas the LCL model estimates harmonic oscillations. This can be due to a higher estimation of turbulent viscosity of the LCL model than the CLS model. However, this difference is not noticeable in μ_t/μ counters but is clear here.

Figure 9 shows the stall effect on pressure coefficient on the airfoil surface. As it is seen, with the increase in the leading angle from 14 to 16, there will be an increase in the value of pressure coefficient as the stall is not occurred yet (especially in the leading edge). But when the leading angle reaches 20° , the value of pressure coefficient drops sharply in the leading edge due to stall. However, a little increase is observed in the trailing edge as well. Finally, the drop in the leading

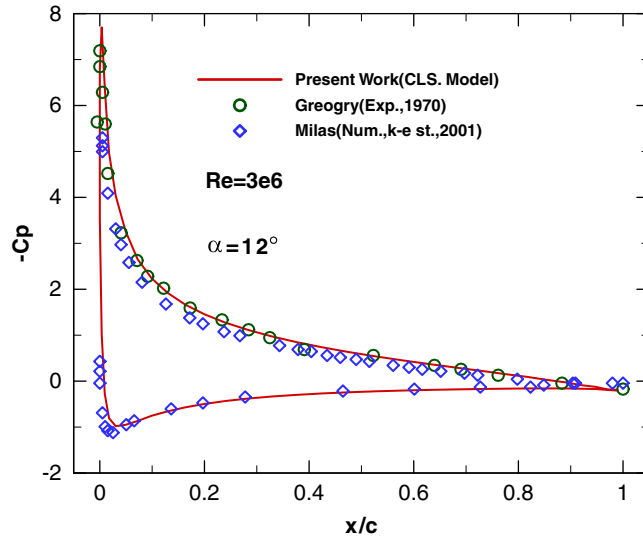


Figure 4. Pressure distribution at $Re = 3 \times 10^6$, $\alpha = 12^\circ$.

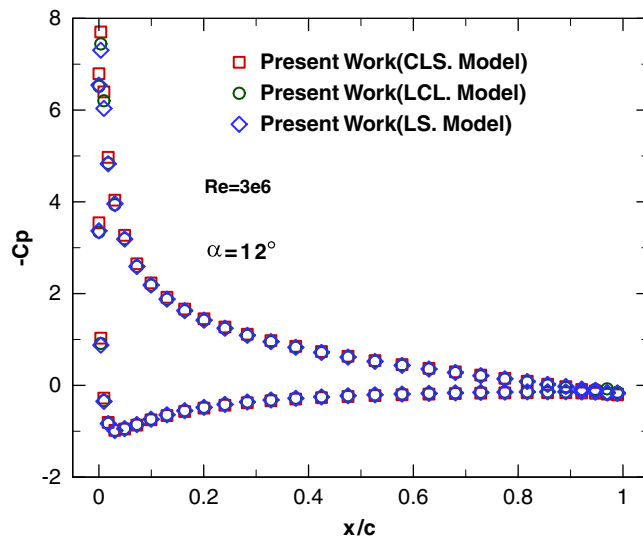


Figure 5. Pressure distribution at $Re = 3 \times 10^6$, $\alpha = 12^\circ$.

edge and the increase in the trailing edge result in a decline in the values of lift coefficient and an increase in the values of drag coefficient in relation to angles before the occurrence of stall.

6.1.2. *Studying flow patterns before and after stall.* In Figure 10, streamlines for the CLS model are shown in Reynolds number of 1×10^6 and 14 and 15° angles in a specific time. As it is seen, a very small vortex has been formed in the 14° leading angle by increasing the leading angle and has moved toward the leading edge along the airfoil surface and it also starts to get bigger. It should be said that this vortex is clockwise. A counterclockwise vortex has been also formed in the trailing edge when the leading angle reaches 16 when the stall occurs. Then, the clockwise vortex gets bigger by increasing the leading angle and another counterclockwise vortex is formed in the trailing edge, which will get bigger by increasing the trailing edge and this process continues.

Figure 11 shows streamlines, turbulent kinetic energy and vorticity for CLS and LS models in the Reynolds number of 1×10^6 and a 20° leading angle in a complete cycle of vortex shedding

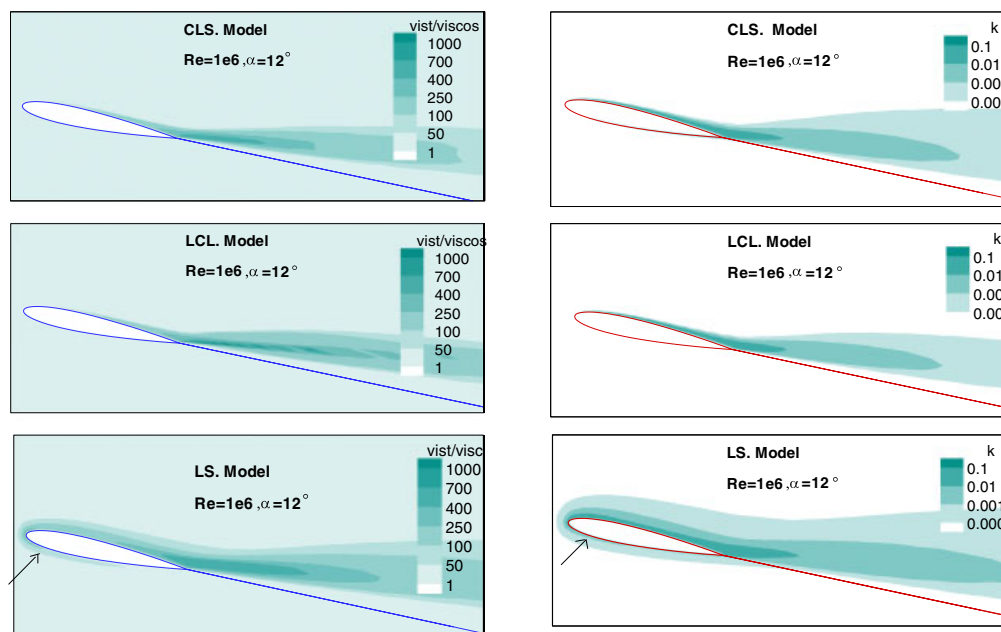


Figure 6. Contours of turbulent kinetic energy and turbulent viscosity to molecular viscosity ratio at $Re = 1 \times 10^6$.

(which leads to a complete oscillation in force coefficients). The period (T) of vortex shedding is obtained using time alternations' diagram of lift and drag coefficients. For a complete cycle of vortex shedding and with time steps of $0.25T$, the contours are presented. The vortex shedding process for the CLS model is explained in the following part.

Given Figure 11, two clockwise vortices (the first and second clockwise vortices from the leading edge of the airfoil, respectively) and a counterclockwise vortex (the first counterclockwise vortex) are seen on the airfoil suction side at $0.0T$. The second clockwise vortex sheds into wake by a $0.25T$ time increase. At the same time, the first vortex enlarges and approaches the trailing edge.

By the further growth of the first vortex and its movement toward the trailing edge at $0.5T$, the first counterclockwise vortex is driven toward the wake and almost separates from the airfoil surface. The first vortex (due to the growth of another vortex in the leading edge) reaches the trailing edge at $0.75T$ and leaves the counterclockwise vortex in the wake completely. The first clockwise vortex is exposed to shedding into wake in $1.0T$ as well and this process continues.

Moreover, given the turbulent kinetic energy counter the CLS model shows the highest value of k in the airfoil wake in a way that the LS model estimated the highest value in the leading edge region in addition to the wake shown in Figure 6.

In Figure 12, averaged turbulent kinetic energy contours and streamlines are presented. Here, interposing was done for 10000 time steps and it is due to nullifying the effect of start and finish points from the vortex shedding cycle. Only two vortices are seen in each of the three models in the flow, one of which is clockwise and the other is counterclockwise. However, it should be noted that clockwise vortices are more elongated in their front part (near the leading edge) in CLS and LCL models, and another clockwise vortex is being formed, which is not detected by the LS model. It seems that the small vortex near the leading edge (which is seen in CLS and LCL models) is dissipated and removed because of the overestimation of turbulent kinetic energy and accordingly, vortex viscosity in the stagnation region and its transmission in the flow line.

6.2. Oscillatory airfoil

In this part, numerical solution results are presented for the 2D and turbulent incompressible flow around an oscillatory NACA0012 airfoil in one Reynolds number of 3×10^6 and one low-Reynolds linear $k-\epsilon$ model (LS) and one low-Reynolds nonlinear $k-\epsilon$ models (CLS).

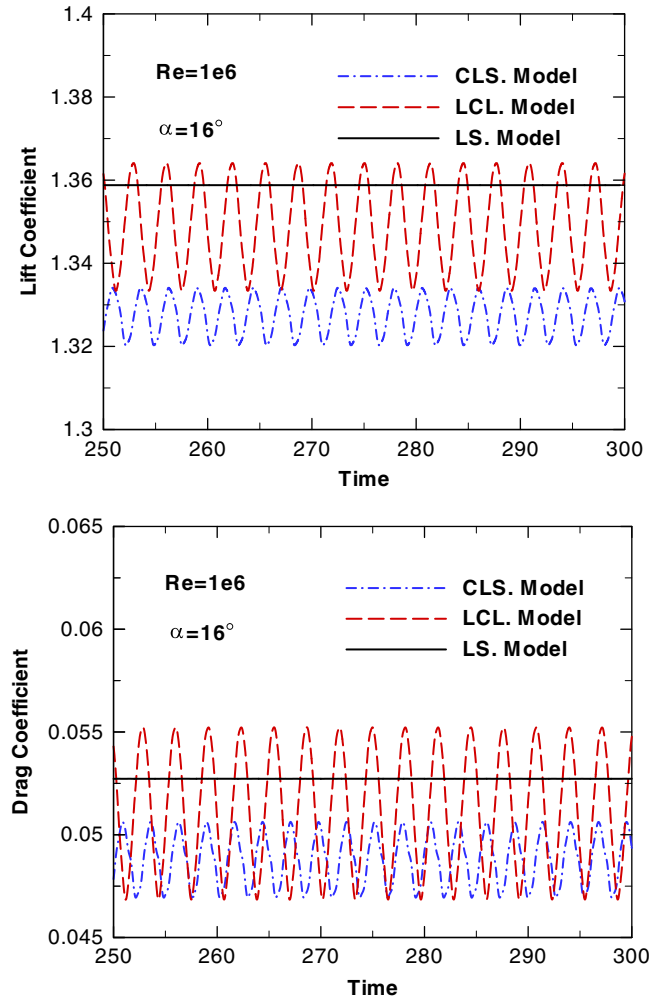


Figure 7. Time history of lift coefficient for an NACA0012 airfoil at $Re = 1 \times 10^6$, $\alpha = 16^\circ$.

Dominant equations, turbulent models, overset grids method and boundary conditions were explained in detail in part one. The vertical oscillation of the airfoil at time t was considered as the function $h = -0.1 \cos(\omega t)$ where ω is the airfoil oscillation frequency. The Reynolds number is considered as 3×10^6 on the basis of airfoil chord and airfoil oscillation is studied in leading angles of 0° , 10° , 17° , 20° and 22° (i.e. chord angle in relation to the free stream flow). It should be mentioned that the airfoil oscillation frequency is expressed by dimensionless reduced frequency, i.e. $k = \omega c / 2U$ in which c is the airfoil chord and U is the free stream flow velocity.

In Figure 13, the airfoil plunging motion equation, velocity, acceleration, the resultant angle of motion and the lift force coefficients are shown. In this diagram, lift force coefficients are used for airfoil in a 0° leading angle. As it is seen, when the effective leading angle of motion is maximum, the lift force coefficient holds its highest value and the velocity value is also maximum at that time.

Figure 14 shows the results of the recent study with CLS and LS models in comparison with reference results [6] in a 0° leading angle and reduced frequency of $k = \omega c / 2U = 0.5$. As seen, there is a good consistency between the values of lift force coefficient and moment coefficient. Given the lift force coefficient diagram, one can say that airfoil oscillation under a plunging function caused the lift force coefficient to oscillate around its value, which is about zero in stationary state as it reaches ± 0.34 under this oscillation. This is due to the fact that the boundary layer flow is more cohesive in the upper surface of airfoil in the plunging motion of airfoil upward as a result

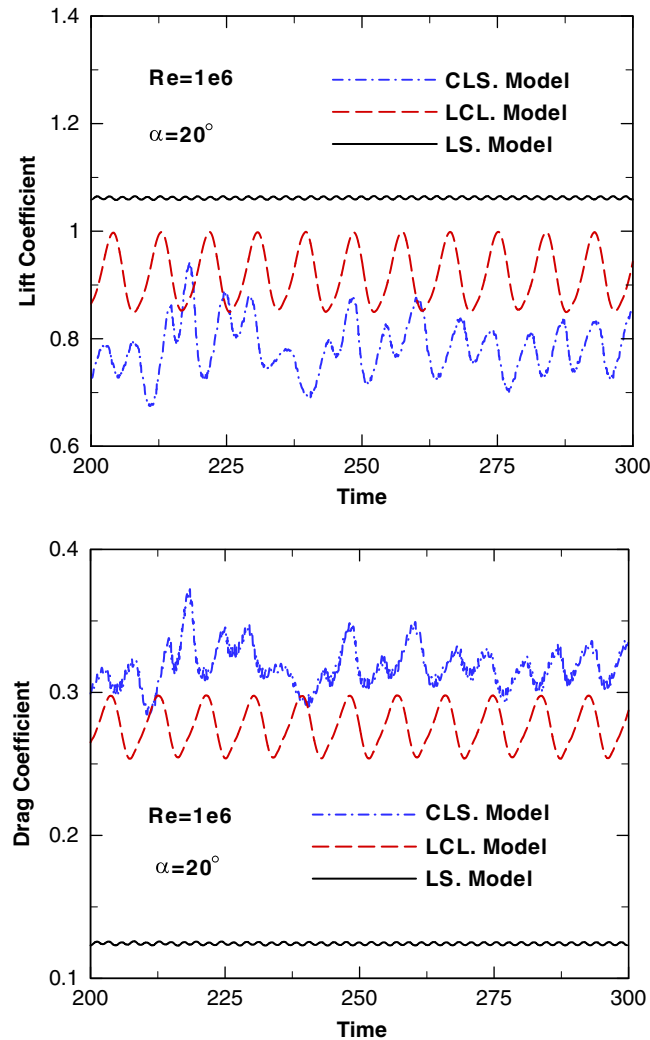


Figure 8. Time history of lift coefficient for an NACA0012 airfoil at $Re = 1 \times 10^6$, $\alpha = 20^\circ$.

of the apparent effects of mass and fluid inertia. Consequently, separation takes place later (wider effective leading angle) and stall is delayed. Accordingly, higher values can be reached in the upstroke motion (which increases the effective leading angle) than in stagnation. On the contrary, lower values can be reached with early separation in the down stroke motion of the airfoil than in stagnation.

Figure 15 presents lift force coefficient changes with the leading angle (α) for the airfoil under plunging oscillation compared with fixed airfoil in the Reynolds number of 3×10^6 . The presented results are for oscillatory airfoil in the reduced frequency of 0.5 and the oscillation amplitude of 0.1. This figure shows maximum, average and minimum values for the lift force coefficient in different leading angles. Comparing the average lift force coefficient for oscillatory and stationary airfoil, it is seen that airfoil oscillation delays flow stall. The oscillatory motion of airfoil delays the stall angle for about 1° and changes the stall from the sudden type to gradual one. It should be noted that airfoil stall in oscillatory state is called dynamic stall.

Figure 16 shows the effect of reduced frequency on force and moment coefficients. Five reduced frequencies are 0.025, 0.05, 0.125, 0.25 and 0.50. Taking the figure into account, it can be seen that force and moment coefficients change a little in the reduced frequency of 0.025 and there are

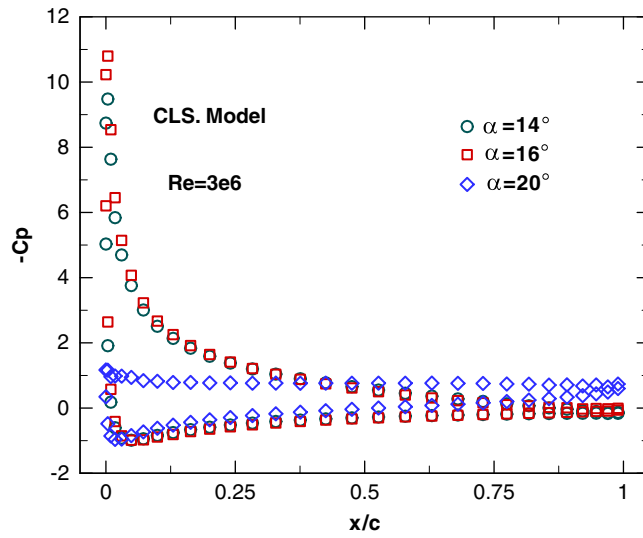


Figure 9. Effect of stall on pressure coefficient at $Re = 3 \times 10^6$.

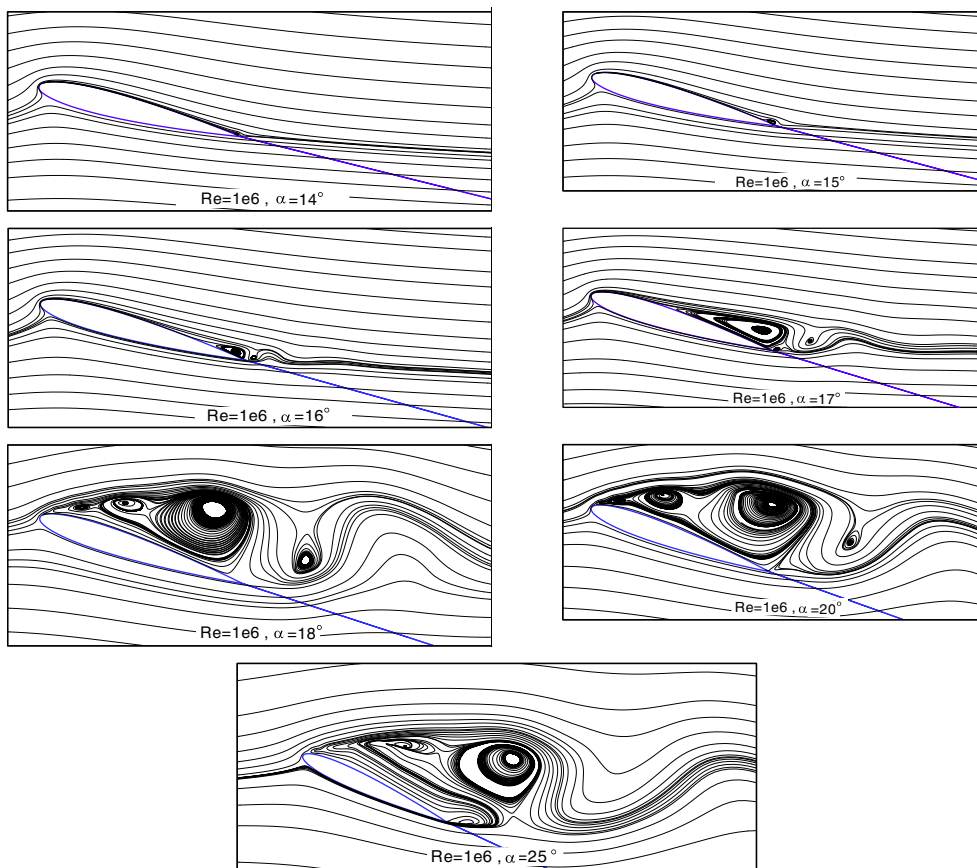


Figure 10. Streamlines around an NACA0012 airfoil using CLS model at $Re = 1 \times 10^6$.

little unsteady effects and indicate semi-constant conditions. Other unsteady effects do not prove little by increasing the reduced frequency. Both frequency and force coefficient amplitude increase under these conditions.

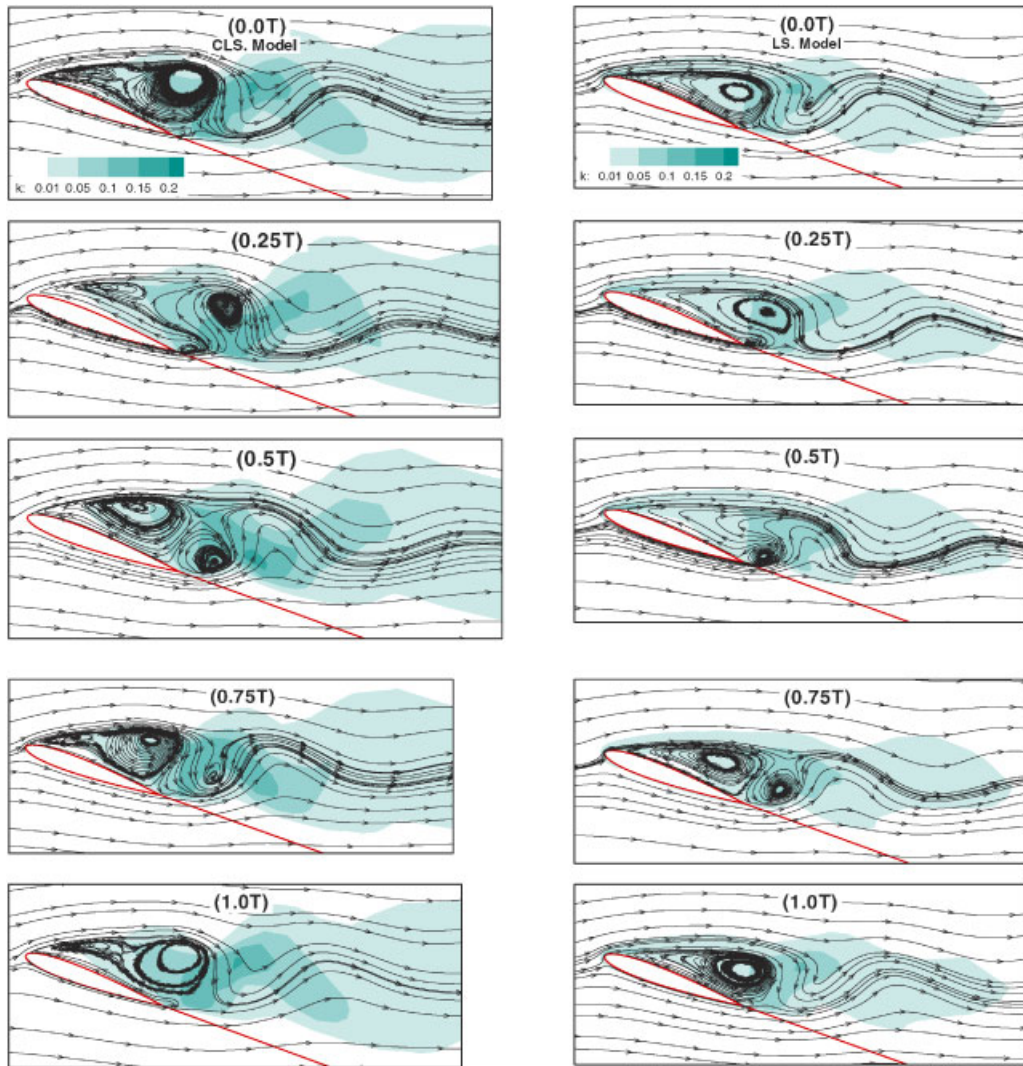


Figure 11. Streamlines and contours of turbulent kinetic energy, CLS model (left), LS model (right) at $Re=1 \times 10^6$, $\alpha=20^\circ$.

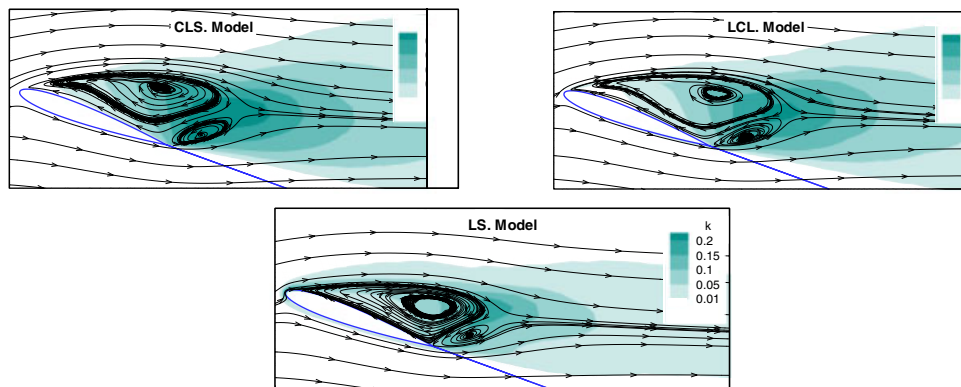


Figure 12. Streamlines and contours of turbulent kinetic energy at $Re=1 \times 10^6$, $\alpha=20^\circ$.

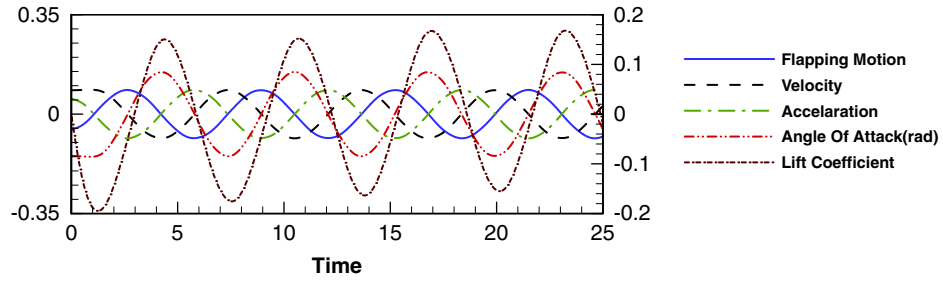


Figure 13. Time history of flapping motion, lift coefficient, velocity and angle of attack.

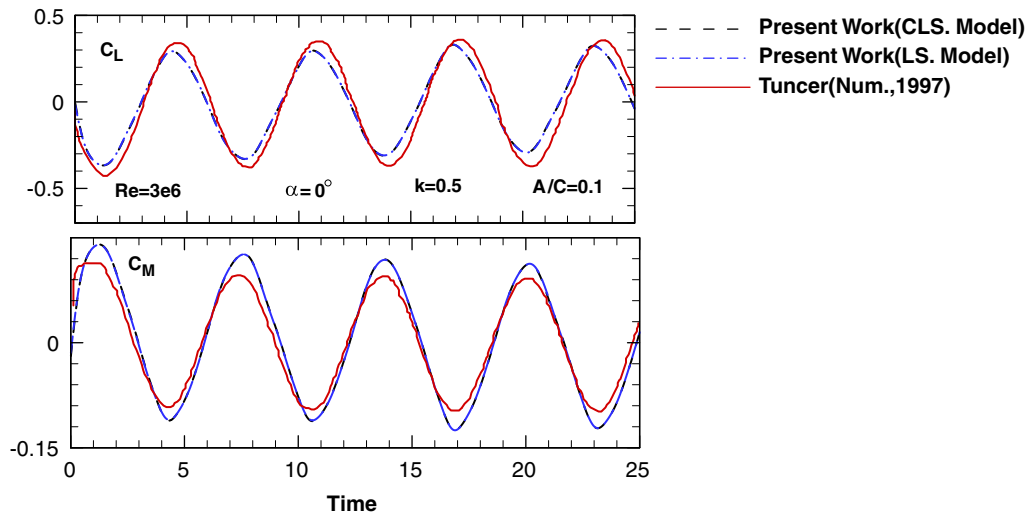


Figure 14. Time history of the unsteady aerodynamic loads, $k=0.5$, $A/C=0.1$, at $Re=3 \times 10^6$, $\alpha=0^\circ$.

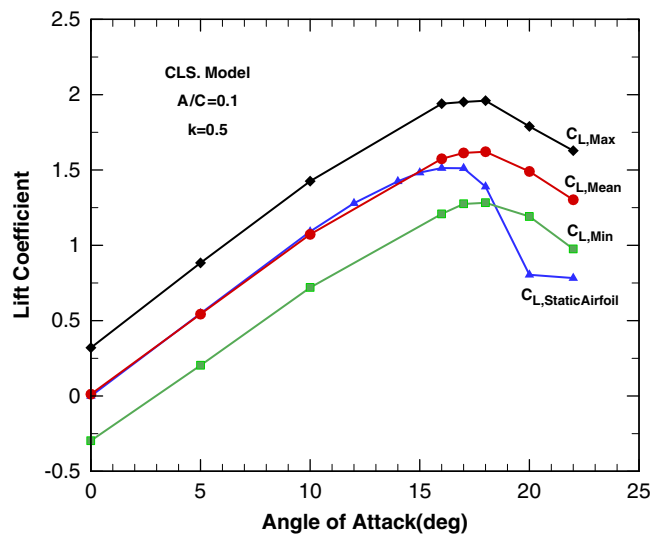


Figure 15. Lift coefficients versus angle of attack in dynamic stall.

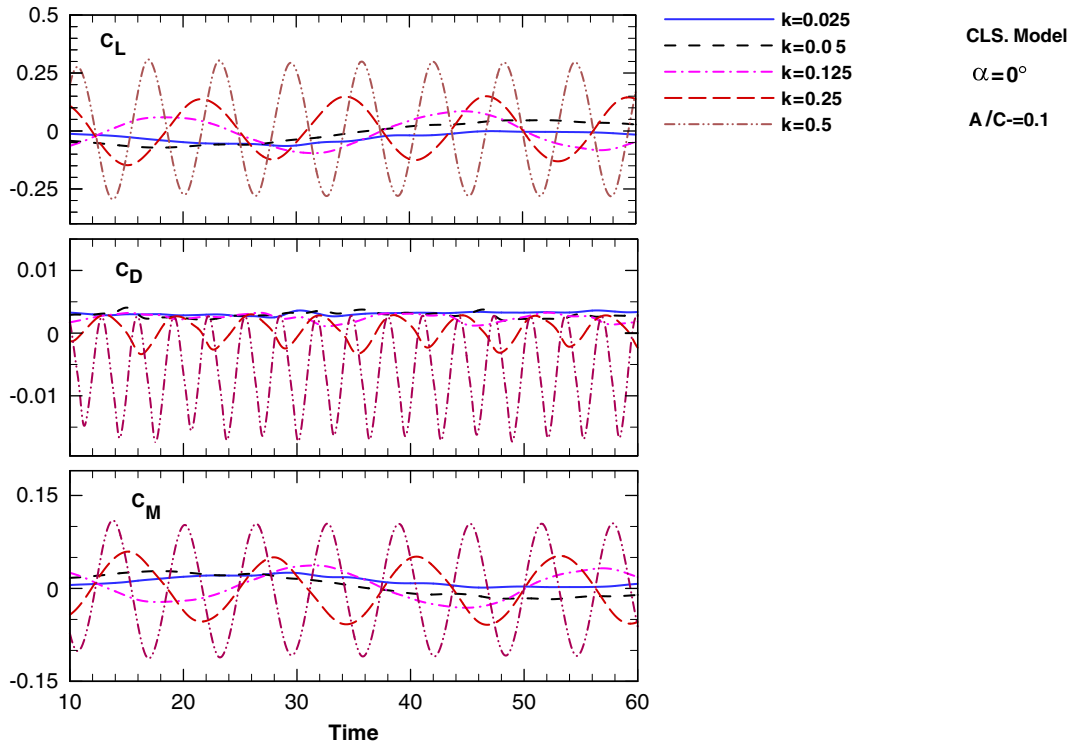


Figure 16. Time history of the unsteady aerodynamic loads, $A/C=0.1$, at $Re=3 \times 10^6$, $\alpha=0^\circ$.

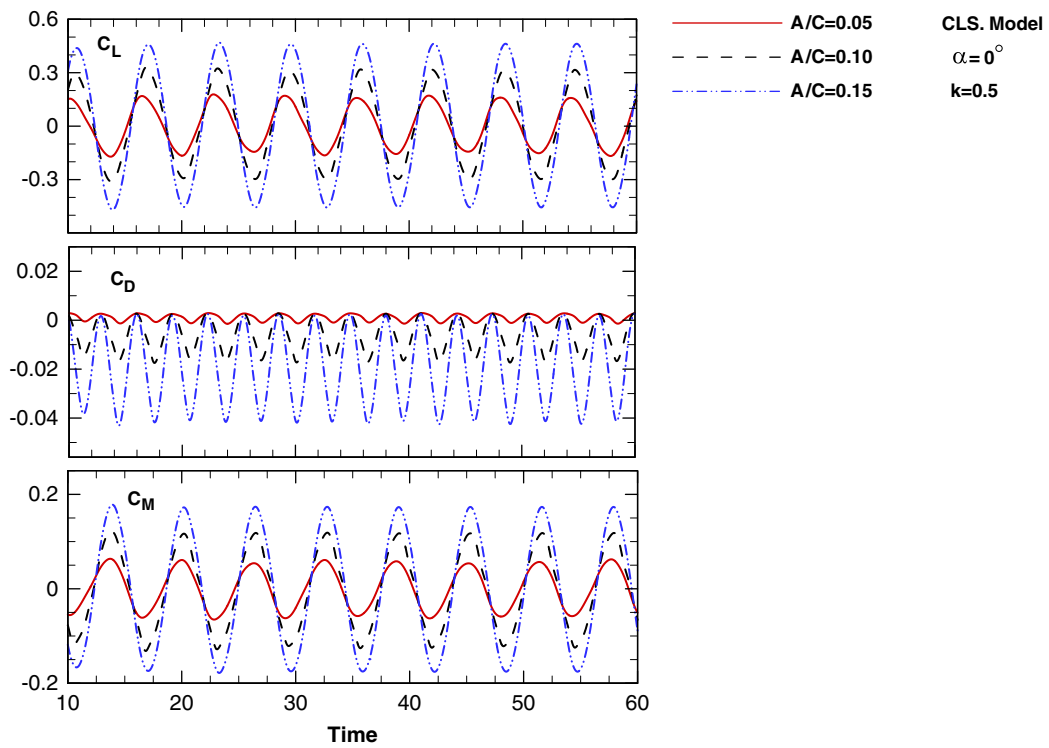


Figure 17. Time history of the unsteady aerodynamic loads, $k=0.5$, at $Re=3 \times 10^6$, $\alpha=0^\circ$.

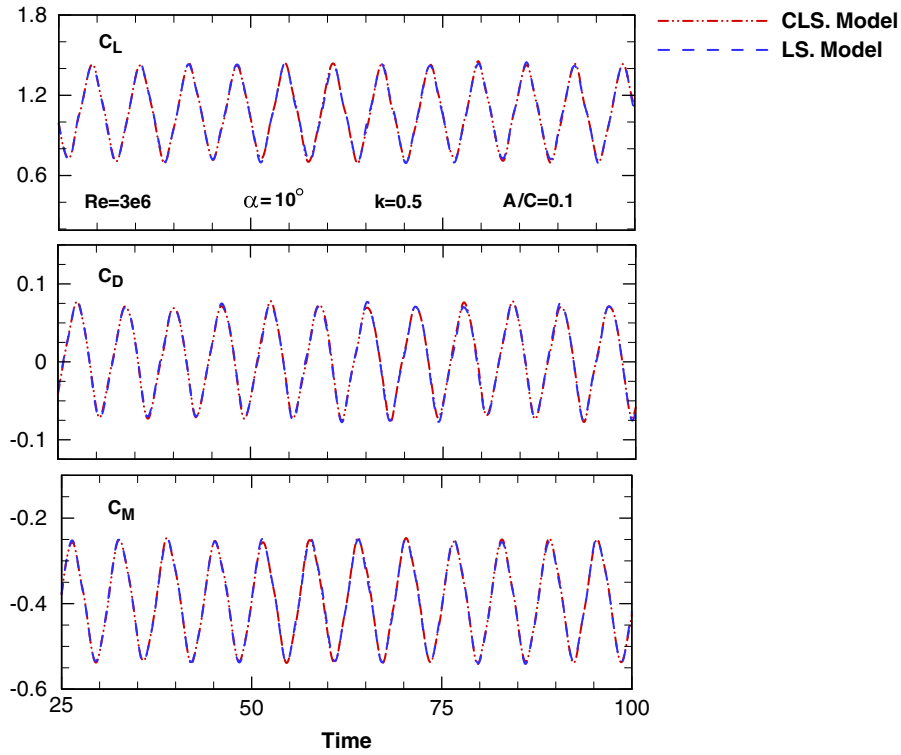


Figure 18. Time history of the unsteady aerodynamic loads, $k=0.5$, $A/C=0.1$, at $Re=3 \times 10^6$, $\alpha=10^\circ$.

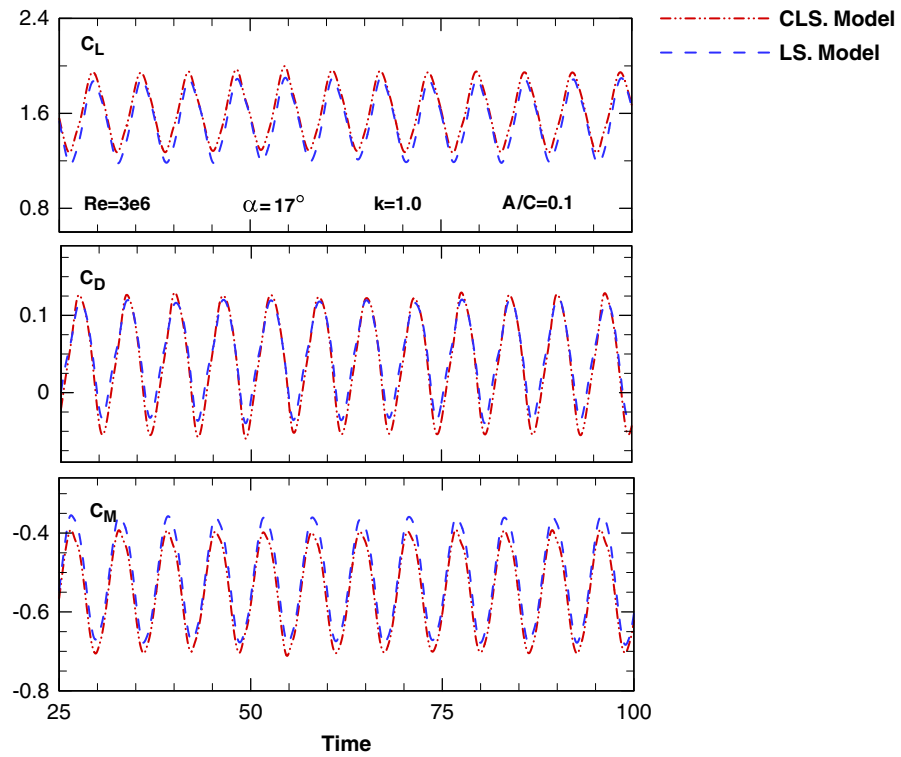


Figure 19. Time history of the unsteady aerodynamic loads, $k=0.5$, $A/C=0.1$, at $Re=3 \times 10^6$, $\alpha=17^\circ$.

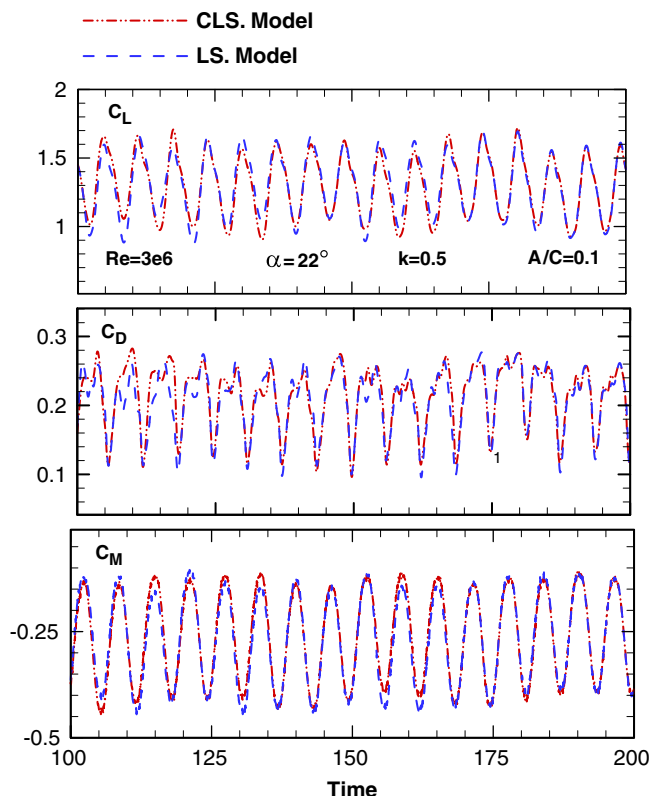


Figure 20. Time history of the unsteady aerodynamic loads, $k=0.5$, $A/C=0.1$, at $Re=3 \times 10^6$, $\alpha=22^\circ$.

Figure 17 studies the effect of airfoil plunging motion amplitude on force and moment coefficients. The results are compared with each other in a 0° leading angle, reduced frequencies of 0.05, 0.1 and 0.15. As it is seen, maximum and minimum values of force and moment coefficients increase by the increase in amplitude. Hence, we can conclude from Figures 4 and 5 that first, the effect of oscillation amplitude increase is more than oscillation frequency and second, the values of force and moment coefficients are also a function of reduced frequency and the plunging motion amplitude of airfoil. Leading angle is not the only determining factor of force coefficients in oscillatory airfoil.

Figures 18–20 present the time alternations of force and moment coefficients for three leading angles of 10° , 17° and 22° , a reduced frequency of 0.5 and an oscillation amplitude of 0.10. As already seen in Section 6.1, there is a great difference in value estimation between LS and CLS models for the 22° leading angle; however, the difference is not noticeable here.

Figure 21 shows streamlines, turbulent kinetic energy counter and vorticity in a 20° leading angle for two LS models. As seen, big vortices, which were formed in the stationary airfoil (Figure 11) [5] of the same leading angle, are not observed here.

7. CONCLUSIONS

In this numerical study, unsteady and incompressible turbulent flows have been considered around stationary and oscillatory airfoils. Overset grid technique is used in this work. Three turbulence models have been examined including the linear LS $k-\varepsilon$ model, nonlinear CLS $k-\varepsilon$ model and nonlinear LCL $k-\varepsilon$ model. The two-dimensional, incompressible governing equations are solved using a finite-volume discretization technique.

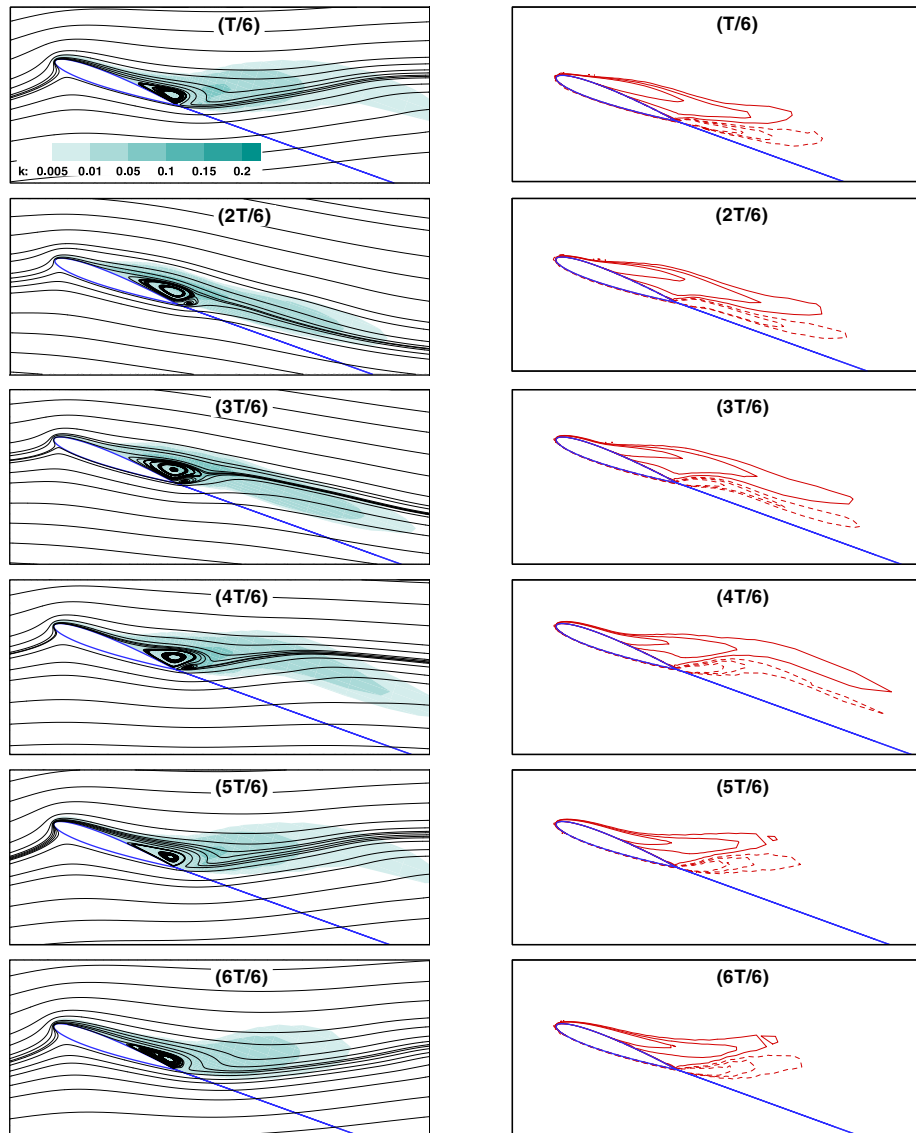


Figure 21. Streamlines and contours of turbulent kinetic energy (left), vorticity (right), CLS model, $k=0.5$, $A/C=0.1$, at $Re=3 \times 10^6$, $\alpha=20^\circ$.

First, the flow field around a stationary airfoil is solved for validating purposes. The results indicate different capabilities to capture separation angle of attack using linear and nonlinear models. Nonlinear models predict smaller stall angle compared with the linear method. Turbulence may be exaggerated within the separation zone and turbulence levels have been overestimated in the boundary layer.

Second, the flow field around an oscillatory airfoil is considered and the effect of the amplitude of oscillation, the frequency and the angle of attack are investigated. Comparing with experiments, it is obvious that the aerodynamic forces and moment are not only a function of the incidence angle but also dependent on oscillatory quantities. The values of the air dynamic forces are also oscillatory around the values obtained for the stationary airfoil. These forces are increased/decreased when the airfoil moves upstroke/down stroke, which is due to the added mass or added inertia. Therefore, the airfoil fluctuations will cause variation in forces and moment as the location of separation zone alters.

REFERENCES

1. Glauert H. Airplane propellers. In *Division L in Aerodynamic Theory*, Durand WF (ed.), vol. IV. Springer: Berlin, 1935; 169–360.
2. Theodorsen T, Garrick IE. Mechanism of flutter, a theoretical and experimental investigation of the flutter problem. *Technical Report, N.A.C.A. Report 685*, 1940.
3. Berton E, Favier D, Maresca C. Embedded L.V. methodology for boundary-layer measurements on oscillating models. *AIAA Paper*, vol. 7(2), 1997; 2106–2116.
4. Panda J, Zaman KB. Experimental investigation of the flow field of an oscillating and estimation of lift from wake survey. *Journal of Fluid Mechanics Digital Archive* 1994; **2**(3): 375–384.
5. Tuncer IH. Unsteady aerodynamics of rapidly pitched airfoil. *AIAA Paper*, vol. 1(2), 1986.
6. Tuncer IH. Two-dimensional unsteady Navier–Stokes solution method with moving overset grids. *AIAA Journal* 1997; **35**(3):2213–2216.
7. Guilmineau E, Queutey P. Numerical study of dynamic stall on several airfoil sections. *AIAA Journal* 1998; **37**(1):128–130.
8. Baracos G, Drikakis D. An implicit unfactored method for unsteady turbulent compressible flows with moving boundaries. *Computers and Fluids* 1999; **28**:899–922.
9. Tuncer IH, Platzer MF. Computational study of flapping airfoil aerodynamics. *Journal of Aircraft* 2000; **37**(3): 2223–2230.
10. Akbari MH, Price SJ. Simulation of dynamic stall for a NACA 0012 airfoil using a vortex method. *Journal of Fluid and Structures* 2003; **3**(2):75–85.
11. Oo GY, Lue KB, Lim TT. Wake structures of a heaving airfoil. *Fifteenth Australian Fluid Mechanics Conference*, The University of Sydney, Sydney, Australia, December 2004; 13–17.
12. Gregory N, O’Riley CL. Low speed aerodynamic characteristics of Naca airfoil section including the effect of upper surface roughness. *NPL AERO Report 1308*, 1970.
13. Abott IH, Doenhoff AE. *Theory of Wing Sections*. Dover: New York, 1958.
14. Michos A, Bergeles G, Athanassiades A. Aerodynamic characteristics of a Naca0012 airfoil in relation to wind generators. *Wind Engineering* 1983; **7**(4):247–262.
15. Sheldahl R, Klimas P. Aerodynamic characteristics of seven symmetrical airfoil sections through 180 degrees for use in aerodynamic analyses of vertical axis wind turbines. *Technical Report SAND80-2114*, Sandia National Laboratories, Australia, 1981.
16. Milas Z. Analysis of turbulent flow around airfoil. *Ph.D. Thesis*, University of Zagreb, Zagreb, 2001; 209.
17. Launder BE, Sharma BI. Application of energy-dissipation model of turbulence to the calculation of flow near a spinning disc. *Letters in Heat and Mass Transfer* 1974; **1**:131–138.
18. Craft TJ, Launder BE, Suga K. Development and application of a cubic eddy-viscosity model of turbulence. *International Journal of Heat and Fluid Flow* 1996; **17**:108–115.
19. Lien FS, Chen WL, Leschziner MA. Non-linear eddy-viscosity modeling of transitional boundary layers pertinent to turbo machine aerodynamics. *International Journal of Heat and Fluid Flow* 1996; **19**:297–306.
20. Jang DC, Jetli R, Acharya S. Comparison of the PISO, SIMPLER, and SIMPLEC algorithms for the treatment of the pressure–velocity coupling in Steady flow problems. *Numerical Heat Transfer* 1986; **10**:209–228.
21. Van Doormaal JP, Raithby GD. Enhancement of the SIMPLE method for predicting incompressible fluid flows. *Numerical Heat Transfer* 1984; **7**:147–163.
22. Leonard BP. A stable and accurate convective modeling based on Quadratic Up-stream Interpolation. *Computer Methods in Applied Mechanics and Engineering* 1979; **19**:59.
23. Crank J, Nicolson P. A practical method for numerical evaluation of solutions of partial differential equations of the heat conduction type. *Proceedings of the Cambridge Philosophical Society* 1947; **43**:50–67. DOI: 10.1007/BF02127704.
24. Thomas JW. *Numerical Partial Differential Equations: Finite Difference Methods*. Texts in Applied Mathematics, vol. 22. Springer: Berlin, New York, 1995; ISBN: 978-0-387-97999-1.
25. Rhie CM, Chow WL. A numerical study of the turbulent flow past an airfoil with trailing edge separation. *AIAA Journal* 1983; **21**(11):1525–1532.
26. Patankar SV. *Numerical Fluid Flow and Heat Transfer*. Hemisphere: New York, 1980.
27. Nirschl H, Dwyer HA, Denk V. Three-dimensional calculations of the simple shear flow around a single particle between two moving walls. *Journal of Fluid Mechanics* 1995; **283**:273–285.
28. Rizzetta DP, Visbal MR. Comparative numerical study of two turbulence models for airfoil static and dynamic stall. *AIAA Journal* 1992; **31**(4): 1514–1522.